Chemical Engineering Journal 496 (2024) 153529

Contents lists available at ScienceDirect

Chemical Engineering Journal

journal homepage: www.elsevier.com/locate/cej

Venice's macroalgae-derived active material for aqueous, organic, and solid-state supercapacitors

Ahmad Bagheri [a,b], Somayeh Taghavi [c], Sebastiano Bellani [d], Pejman Salimi [e,f], Hossein Beydaghi [d], Jaya-Kumar Panda [d], Marilena Isabella Zappia [d], Valentina Mastronardi [d], Agnese Gamberini [d], Sanjay Balkrishna Thorat [d], Matteo Abruzzese [d], Lea Pasquale [g], Mirko Prato [g], Michela Signoretto [h], Xinliang Feng [b,i], Francesco Bonaccorso [a,d,*]

[a] Graphene Lab, Istituto Italiano di Tecnologia, Via Morego 30, 16163 Genoa, Italy
[b] Center for Advancing Electronics Dresden (cfaed) & Faculty of Chemistry and Food Chemistry, Technische Universität Dresden, 01062 Dresden, Germany
[c] Faculty of Chemistry, University of Mazandaran, 47416-95447 Babolsar, Iran
[d] BeDimensional S.p.A., Lungotorrente Secca 30R, 16163 Genoa, Italy
[e] Analytical and Circular Chemistry (ACC), Hasselt University, Hasselt, Belgium
[f] Institute for Materials Research (imo-imomec), Hasselt University, Hasselt, Belgium
[g] Materials Characterization Facility, Istituto Italiano di Tecnologia, Via Morego 30, 16163 Genova, Italy
[h] CATMAT Lab, Department of Molecular Sciences and Nanosystems, Ca' Foscari University Venice and INSTM Consortium, RU of Venice, Via Torino 155, 30172 Venezia Mestre, Italy
[i] Max Planck Institute of Microstructure Physics, Weinberg 2, 06120 Halle, Germany

ARTICLE INFO

Keywords:
Activated biochar
Electrolyte
Physical activation
Solid-state supercapacitors
Energy storage

ABSTRACT

In this study, self-doped porous activated biochar derived from Venice lagoon's Sargassum brown macroalgae (ABS) has been successfully prepared through thermochemical carbonization (pyrolysis) followed by CO_2 physical activation and used as electrodes for supercapacitor (SC) applications. The ABS exhibits a remarkable specific surface area of 821 m^2g^{-1} and heteroatoms (N, O, and S) doping, both key features to attain high-performance carbon-based SC electrodes. The electrochemical performances of ABS-based SCs were assessed in three different electrolytes. Two are aqueous (i.e., 1 M H_2SO_4 and 8 M $NaNO_3$), while the third one is the prototypical organic, namely 1 M $TEABF_4$ in acetonitrile. In these three electrolytes, the ABS-based electrodes exhibited specific capacitance values (C_g) of 109.5, 79.0, and 64.3Fg^{-1}, respectively, at a current density of 0.1 Ag^{-1}. The capacitive performance resulted in SC energy densities of 3.45 Wh kg^{-1} at 22.5 W kg^{-1}, 6.3 Wh kg^{-1} at 36.1 W kg^{-1}, and 12.4 Wh kg^{-1} at 57.4 W kg^{-1} and maximum power densities of 147, 222, and 378 kW kg^{-1} in the acidic, quasi-neutral aqueous electrolyte and organic electrolyte, respectively. The ABS electrodes were used to realize a flexible solid-state SC based on the sulfonated polyether ether ketone (SPEEK):functionalized niobium disulfide flakes (f-NbS_2) composite membrane. The flexible solid-state SC displayed a remarkable 97% C_g retention even under various mechanical stresses, including bending up to 1000 times and folding angles up to 180°, while keeping a Coulombic efficiency above 98%. This study reveals ABS as a promising sustainable source of active materials for SCs. The remarkable performance of ABS-based SCs can be attributed to their multi-scale porosity, heteroatom doping, and enhanced surface wettability, providing abundant active sites for charge accumulation, and efficient electrolyte diffusion, thus highlighting its potential as a sustainable solution for energy storage applications.

1. Introduction

Sustainable energy storage and conversion technologies must be developed to meet rising energy consumption while tackling climate change, environmental pollution, and biodiversity loss [1–3]. In this context, supercapacitors (SCs) represent electrochemical energy storage systems that combine the advantages of traditional capacitors and batteries by storing energy through electrostatic double-layer capacitance

* Corresponding author at: Graphene Lab, Istituto Italiano di Tecnologia, via Morego 30, 16163 Genoa, Italy..
E-mail address: f.bonaccorso@bedimensional.it (F. Bonaccorso).

https://doi.org/10.1016/j.cej.2024.153529
Received 31 March 2024; Received in revised form 20 June 2024; Accepted 25 June 2024
Available online 28 June 2024

and faradaic pseudocapacitance mechanisms [4–6]. With excellent rate capability, *i.e.*, specific power (P_s) exceeding 10 kW kg^{-1} and long cycle life (up to millions of charge/discharge −CD- cycles regardless of the depth of discharge), SCs outperform common battery technologies in terms of round trip efficiency, longevity (*e.g.*, 20 years lifespan), and power densities. These distinguishable features make SCs a compelling choice to efficiently and rapidly match the energy demand, as well as to control the ramp up or down of the energy supplied by renewable technologies in distributed (decentralized) renewable energy systems [7,8]. Furthermore, SCs operate efficiently within a wide temperature range, *i.e.*, from −40 °C to 80 °C, making them adaptable to/reliable in extreme environments, *e.g.*, Arctic and deserts [9,10]. The SCs are commonly classified into three main categories: electrical double-layer capacitors (EDLCs), pseudocapacitors, and hybrid SCs (HSCs). Commercial SCs are mainly EDLCs based on high-surface carbon electrodes, which are charged/discharged *via* ion adsorption/de-adsorption processes at the electrode–electrolyte interfaces [10–12]. Activated carbon (AC), carbon nanotubes, and graphene have been widely used as active materials for EDCL electrodes due to the combination of high electrical conductivity, large specific surface area, and excellent chemical stability [5,13–15]. Even though AC still represents the most economically viable active material choice amongst the aforementioned materials, marketable products are commonly derived from fossil fuel precursors, increasing the cost (up to $5000–100000 per kWh) and environmental impact of EDLCs [16]. Recently, the use of biomasses to produce AC, *e.g.*, by upcycling waste materials, has been considered a suitable cost-effective strategy that preserves the ecological balance. Examples of biological precursors for AC are rice husk [17], silk cocoon [18], and algae [19]. Specifically, Algae, unlike land plants, can form massive populations in coastal areas on all continents, but also off-shore in tanks, ropes, and other supports in marine systems, *e.g.*, offshore wind parks [20,21]. They also have the ability to thrive in various aquatic environments, including salt water, spurring seaweed farming that does not rely on energy-intensive farming practices and does not compete for freshwater resources, resulting in the production of “truly green” biomasses [22]. The accumulation of a large amount of proteins and lipids within their cellular biomass is the source of N and S heteroatoms [23], which, in turn, can be used to produce heteroatom-doped biochar through pyrolysis processes. During pyrolysis, these biomasses convert to heteroatom as dopants into the carbon matrix without the need for extra chemical reagents [24]. Heteroatoms like N, O, S, and P efficiently enhance the electrical conductivity and wettability of algae-derived biochar [25]. Heteroatom insertion primarily occurs at the outer region of the carbon sheets, while the internal region undergoes a process called localized crystallization [26], resulting in an ordered structure. This ordered structure significantly enhances porosity, which is crucial for energy storage applications [27]. Activation techniques, including chemical or physical activations and template-assisted methods, can be used to increase the specific surface area (up to ~ 3000 m^2g^{-1}) and porosity (even up to > 1 $cm^3\ g^{-1}$) of biochars [27,28]. More in detail, high-temperature physical activation can break crosslinks between carbon sheets, resulting in the formation of free carbon layers that are conductive and incorporate heteroatoms [29]. The heating process preserves the original morphology of carbon, while gases escape, forming pores and channels [30]. Chemical activation using chemical etching agents, *e.g.*, $ZnCl_2$, KOH, and HNO_3, leads to porous carbons with high specific surface area and highly developed pore structure [29,31]. Furthermore, physical activation methods, involving steam [30], carbon dioxide (CO_2) [26], or air [32], can enlarge the volume of pores in biochars, promoting the formation of hierarchically porous structures at nano, micro, and macro scales (microporosity, mesoporosity, macroporosity, respectively). In general, physical activation methods are also cheaper and safer than chemical activation treatments involving high-temperature conditions with a significant environmental footprint [29–31].

Herein, algal biomass, namely *Sargassum* brown macroalgae from Venice Lagoon, was used as a biosource for the preparation of biochar. The widespread distribution of *Sargassum,* as well as the bloom of other algae, in Venice Lagoon results from the eutrophication of the lagoon, *i.e.*, enrichment of N- and P-rich nutrients, associated to the morphological and hydrodynamic setting of the lagoon. The blooms of macroalgae and their subsequent decomposition have been typically associated to negative effects, *i.e.*, anoxia in large parts of the Venice lagoon that causes mass mortality of benthic animals and fish, coral reef destruction and toxin release [33]. Thus, the use of algae for the preparation of biochar as a precursor of SC active materials can be considered as an environmentally friendly approach to produce valuable products, while restoring and/or safeguarding the balance of marine ecosystem negatively affected by human economic activities. The localized graphitic order and the textural properties of *Sargassum*-derived biochar were then modified by a physical activation process using CO_2 as an activation agent [26]. The effect of functional groups on the electrochemical performance of the N, O, S-self-doped-activated biochar derived from *Sargassum* (ABS) was investigated in SCs based on various types of electrolytes, including prototypical organic (1 M tetraethylammonium tetrafluoroborate −$TEABF_4$- in acetonitrile −ACN-) and aqueous (1 M H_2SO_4 and 8 M $NaNO_3$) ones, reaching specific energies (Es) up to 12.4 Wh kg^{-1} at 57.4 W kg^{-1}, 3.45 Wh kg^{-1} at 22.5 W kg^{-1}, and 6.35 Wh kg^{-1} at 36.1 W kg^{-1}, respectively. Furthermore, flexible solid-state SC (FSSSC) was also constructed by combining the designed ABS-based electrodes with a solid-state electrolyte (SSE), namely a sulfonated polyether ether ketone (SPEEK):functionalized niobium disulfide flakes (f-NbS_2) composite membrane developed in ref. [34]. The as-produced FSSC exhibited an Es of 5.8 Wh kg^{-1} at 87.4 W kg^{-1}, retaining its performance after several bending cycles (up to 1000 cycles) and during folding conditions. The validation of ABS in different SC configurations opens the way toward sustainable use of marine biomasses for electrochemical energy storage applications.

2. Results and discussion

Scheme 1 represents the synthesis and activation method used to produce ABS (see details in Supporting Information).

Fig. 1a reports the Fourier-transform infrared spectroscopy (FTIR) spectrum of ABS, showing the presence of various functional groups. The band at around 3400 cm^{-1} is associated with hydroxyl group vibrations [35]. The band at 1600 cm^{-1} is related to the stretching vibration of aromatic C=C and stretching of C=O from conjugated ketones and quinones [36]. Moreover, a wide peak in the range of 1400–900 cm^{-1} is a series of overlapping bands likely ascribed to O-, N-, S-based dopants and functional groups in ABS, including C–O bonds in phenol, alcohol, bridging ether between aromatic rings, N–COO and N–C groups, S–O in sulfonate, S=O in sulfuric acid, SO_2 in sulfonic acid and sulfone, respectively [37]. The bands at 2850, 2920, and 800 cm^{-1} are associated with aliphatic (alkenes) and aromatic C–H, respectively [38]. The specific peaks corresponding to the various functional groups are reported in Table S1. Fig. 1b shows the X-ray diffraction (XRD) pattern measured for the ABS. This pattern exhibits two prominent peaks at 2θ values of approximately 25° and 44°, corresponding to the (0 0 2) and (1 0 0) reflections of a disordered turbostratic carbon (or hard carbon) structure, respectively [39]. In particular, according to Bragg’s law [26], the interlayer distance between the graphitic layers (d_{002}) of ABS is calculated to be ~ 0.357 nm, which is larger than the d-spacing of graphite (0.335 nm) [40,41]. The increased interlayer spacing and the presence of turbostratic disorder in ABS suggest enhanced electrochemical properties, including higher ion accessibility and improved charge storage capabilities, which are beneficial for applications like SCs. Fig. S1 presents the XRD pattern of the biochar, which behaves like disordered turbostratic carbon structure. As for the activated counterpart, two broad diffraction peaks at 2θ values of approximately 23.5° and 43° correspond to the (0 0 2) and (1 0 0) reflections. The difference in the (0 0 2) peak positions between the biochar and the ABS indicate

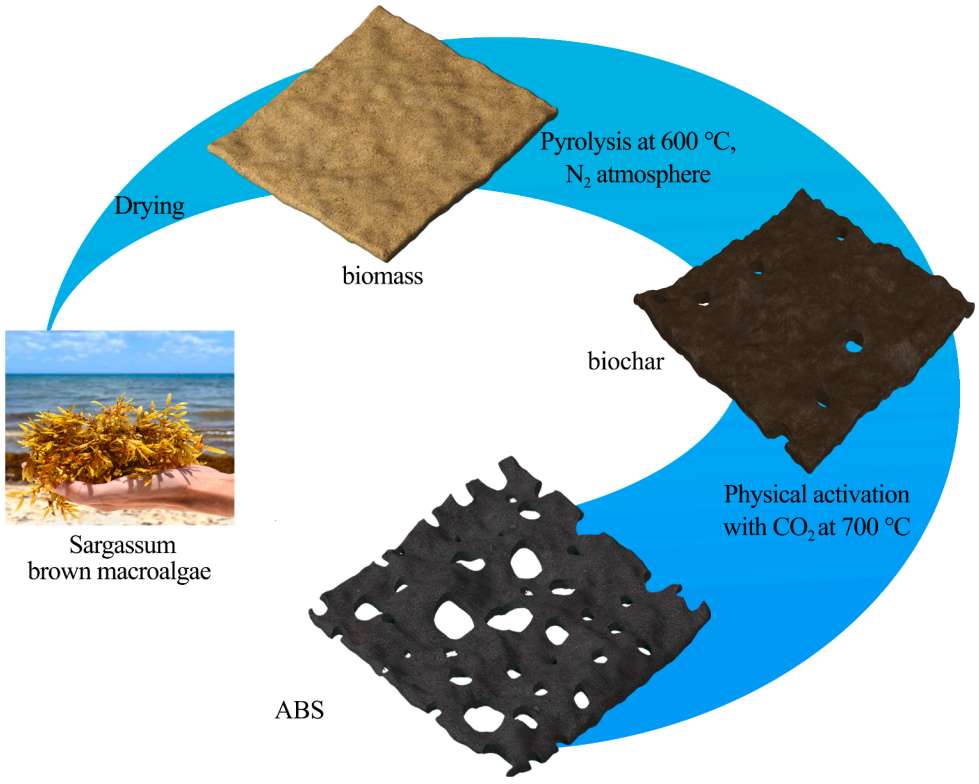

Scheme 1. Production of ABS through the activation of *Sargassum* brown macroalgae-derived biochar.

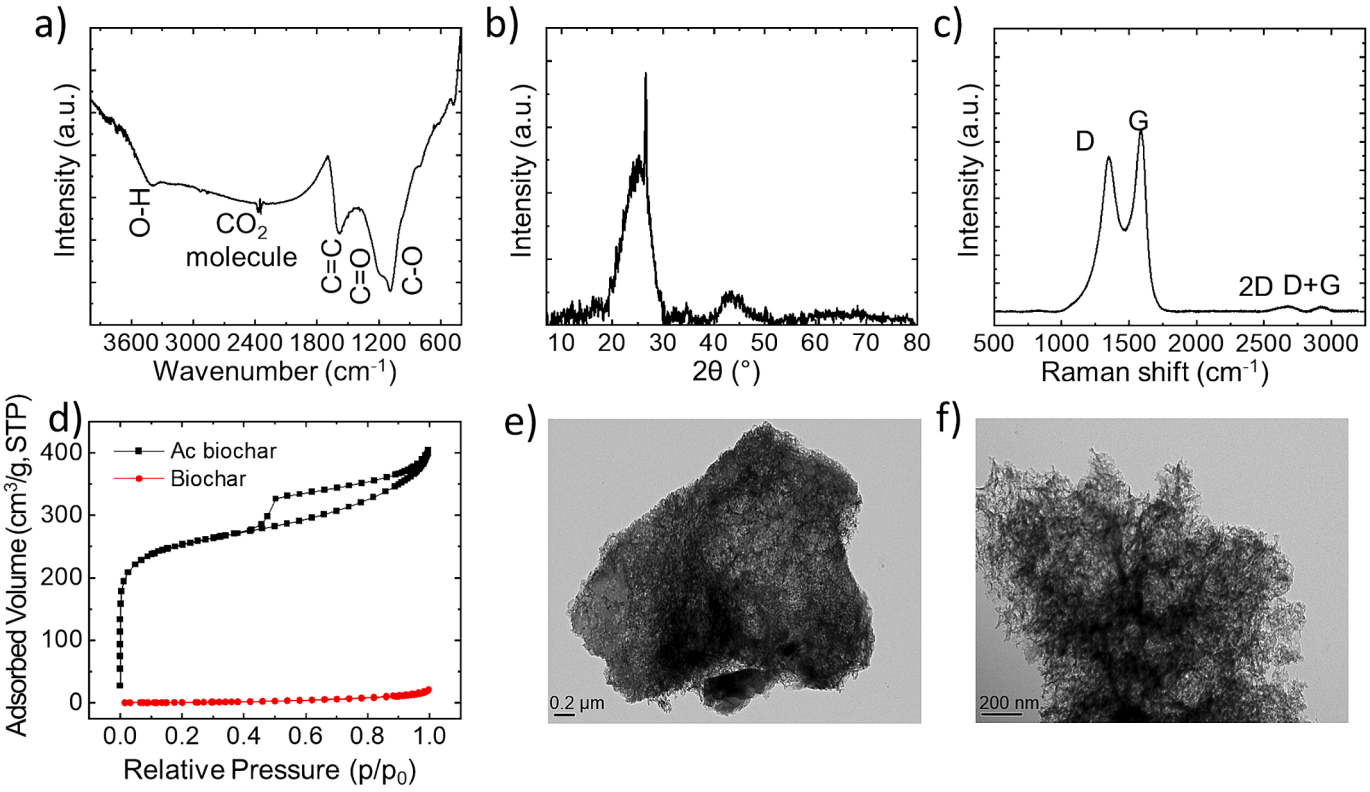

Fig.1. Structural and morphological characterization of ABS. (a) FTIR spectra, (b) XRD pattern, and (c) Raman spectrum measured for ABS. (d) N_2 adsorption–desorption isotherms measured for *Sargassum* brown macroalgae-derived biochar and ABS. TEM images of (e) ABS and (f) a magnified area showing the material porous structure.

different d_{002}, which is larger for the former (~0.378 nm). In addition to the (0 0 2) and (1 0 0) reflections, several sharp peaks are present in the XRD patterns. Notably, the sharp peak at 27° can be ascribed to some inorganic phases including crystalline SiO_2 (quartz (ICSD 83849), and Trydimite (ICSD 176)), typical contaminations present in quartz reactors which cannot be removed during the HCl acid-washing step [26].

Raman spectroscopy analysis was also performed to elucidate the structural order of ABS. The Raman spectrum of ABS (Fig. 1C) exhibits distinct bands. The D band, located around 1360 cm^{-1}, is associated with defects in graphitic structure and disorder, while the G band around 1600 cm^{-1} corresponds to the graphitic layers and shows in-plane vibrational mode of sp^2-hybridized carbon atoms [42,43]. The band at ca. 2650 cm^{-1} is the overtone of D band and is denoted as 2D [44]. Lastly, the band peaked at ca. 2950 cm^{-1} is associated with a D + G combination mode [45]. The ratio between the intensity of D-band and G-band (I_D/I_G) was used to evaluate the degree of graphitization [43,46]. In this study, the I_D/I_G value is approximately 0.86. This ratio closely resembles values reported for other activated biochars in literature [36,47].

Fig. 1d reports the N_2 adsorption–desorption isotherm measured for the ABS. A combination of type I and type IV isotherms indicates the presence of a hierarchical micro-mesoporous texture. In particular, the initial uptake of volume adsorbed at $P/P_0 < 0.2$ suggests the presence of micropores, while the hysteresis loop at $0.4 < P/P_0 < 0.99$ is associated with the existence of narrow slit-shaped mesopores (see Fig. S2 for pore size distribution). Similar results were obtained for activated biochars produced by pyrolysis and physical activation (H_2O, and H_2O/CO_2 as the activation agents) of *Sargassum* [30]. Table 1 reports the textural properties of ABS including Brunauer–Emmett–Teller (BET) specific surface area (S_{BET}) calculated by BET method for multilayer adsorption considering interactions between adsorbed molecules (N_2) within each layer. Additionally, it includes the Langmuir specific surface area ($S_{Langmuir}$), determined by the Langmuir method for monolayer adsorption, where no interaction among adsorbed molecules is considered, and the specific micropore surface area (S_{micro}), calculated using the t-plot method. Notably, ABS exhibits a substantial S_{BET} of 821 m^2g^{-1}, $S_{Langmuir}$ of 1305 m^2g^{-1}, and S_{micro} of 905 m^2g^{-1}, indicative of a hierarchical micro-mesoporous texture characterized by a specific micropore volume (V_{micro}) of 0.17 $cm^3\ g^{-1}$, constituting 30% of the total pore volume (V_{tot} = 0.56 $cm^3\ g^{-1}$). Remarkable specific surfaces areas and mesoporosity (V_{meso} = 0.39 $cm^{-3}g^{-1}$, mean pore diameter (d_p) = 4.9 nm) of ABS are attributed to both the characteristics of the native *Sargassum* biomass and its activation treatment. Importantly, ABS exhibits superior specific surface area and mesoporosity compared to other biochars derived from various biomasses (including leather tannery waste, barley waste, and vine wood waste) and activated like our ABS [48]. The distinctive textural properties of ABS can therefore be associated with the peculiar composition of *Sargassum* biomass, which is notably rich in proteins and lipids. During the thermal carbonization process under inert atmosphere, biomasses release heteroatoms from their macromolecules' backbones, evolving into porous carbon skeletons [49]. Subsequent activation processes further refine these structures, resulting in a conductive 3D frameworks with hierarchical porosity and high specific surface area suitable for SC applications [36,49]. It is well-documented that high-specific surface area carbons featuring hierarchical pores provide abundant sites for electrolyte ions adsorption and infiltration, facilitating rapid ion transport and diffusion during discharge/charge processes [18,50]. In particular, micropores ensure high specific surface area which result in high capacitance, while the presence of mesopores minimizes ion diffusion distance to achieve high rate capability [18,51].

Fig. 1e-f shows the transmission electron microscopy (TEM) images of the ABS, revealing a porous structure, as confirmed by gas physisorption measurements. Although the biochar mineral skeleton is preserved, some mass is lost during the activation process, leading to enhanced porosity.

Scanning electron microscopy (SEM) images were carried out to further evaluate the surface morphology of ABS (Fig. 2). As shown in Fig. 2a, in some parts of its surface, the ABS shows a beehive-like network made of pores and inner channels. A similar morphology has been observed for biochars obtained from lignocellulosic biomasses due to the presence of carbohydrates [52], which are also present in *Sargassum* brown macroalgae. Other parts of the ABS surface exhibit a rough and irregular porous surface, leading to a heterogeneous morphology associated with the presence of high ash content in activated biomass-derived chars (Table S2).

The energy dispersive X-ray (EDX) spectrum and element mapping of the ABS are shown in Fig. 2b-c, respectively, showing uniform element distributions. The compositional analysis (inset table to Fig. 2b) and CHNS elemental analysis (Table S2) confirm the presence of O, N, and S heteroatoms, acting as dopants of forming functionalities in ABS obtained by carbohydrate-, protein- and lipid-containing *Sargassum*. Furthermore, Fig. S3 provides supplementary SEM-EDS analysis with a different magnification, highlighting the presence and distribution of these elements, as well as C, P, and Si. The surface chemical composition of the ABS was evaluated by X-ray photoelectron spectroscopy (XPS) and the atomic ratios of C, O, N, and S (Table S3) were extracted from the wide scan XPS spectrum (Fig. 3a). Silicon peaks are visible at approximately 100 and 150 eV and are attributed to contamination in the sample, as often observed for materials activated in quartz reactors. Fig. 3b-e reports the high-resolution N 1s, C 1s, S 2p, and O 1s XPS spectra. The N 1s spectrum (Fig. 3b) can be deconvoluted into five peaks: pyridinic-N (398.2 ± 0.2 eV), amino/amide-N (399.5 ± 0.2 eV), pyrrolic-N (400.1 ± 0.2 eV), quaternary-N (401.0 ± 0.2 eV), and oxidized-N (402.4 ± 0.3 eV) [53]. The C 1s spectrum (Fig. 3c) is instead deconvoluted into seven peaks centered at (283.6 ± 0.2) eV, (284.5 ± 0.2) eV, (284.8 ± 0.2) eV, (286.3 ± 0.2) eV, (287.8 ± 0.2) eV, (289.3 ± 0.2) eV, and (291.0 ± 0.2) eV, corresponding to C vacancies, C=C (sp^2-hybridized carbon), C-C (sp^3-hybridized carbon), C-O/C-OC and/or C=N linkage (phenolic hydroxyl/epoxy), C=O (carbonyl) and/or C-N and O=C-O (carboxyl groups and/or ester groups), and π-π* satellite peak, respectively [54]. In the S 2p spectrum (Fig. 3d), two different doublets are associated with different chemical states, *i.e.*, thiol groups (S 2p doublet with components peaking at 163.7 ± 0.2 for S $2p_{3/2}$ and 164.9 ± 0.2 eV for S $2p_{1/2}$) and sulfates (S 2p doublet with components peaking at 167.7 ± 0.2 for S $2p_{3/2}$ and 168.9 ± 0.2 eV for S $2p_{1/2}$). These two S chemical states have been respectively associated with the presence of the cysteine and sulfated polysaccharides, as present in the *Sargassum* precursor [23]. Note that a Si plasmon loss peak is present at (164.9 ± 0.2) eV and it has been considered in the deconvolution process. Lastly, the O 1 s spectrum (Fig. 3e) can be deconvoluted into four components corresponding to C = O (531.3 ± 0.2 eV), S-O (532.3 ± 0.2 eV), O-C=O/−OH (532.9 ± 0.2 eV), and − COOH (534.7 ± 0.2 eV) groups [55]. The presence of localized density of states (DOS) near the Fermi level has been documented [56,57] for active materials containing pyridinic N, which may consequently improve the quantum capacitance of undoped counterparts. More in details, this improvement arises from the increased availability of electronic states for charge storage.

Table 1
Textural properties of ABS obtained from N_2 physisorption measurements.

Sample	S_{BET} (m^2g^{-1})	$S_{Langmuir}$ (m^2g^{-1})	S_{micro} (m^2g^{-1})	V_{tot} (cm^3g^{-1})	V_{micro} (cm^3g^{-1})	V_{meso} (cm^3g^{-1})	d_p (nm)
Activated biochar	821	1305	905	0.56	0.17	0.39	4.90

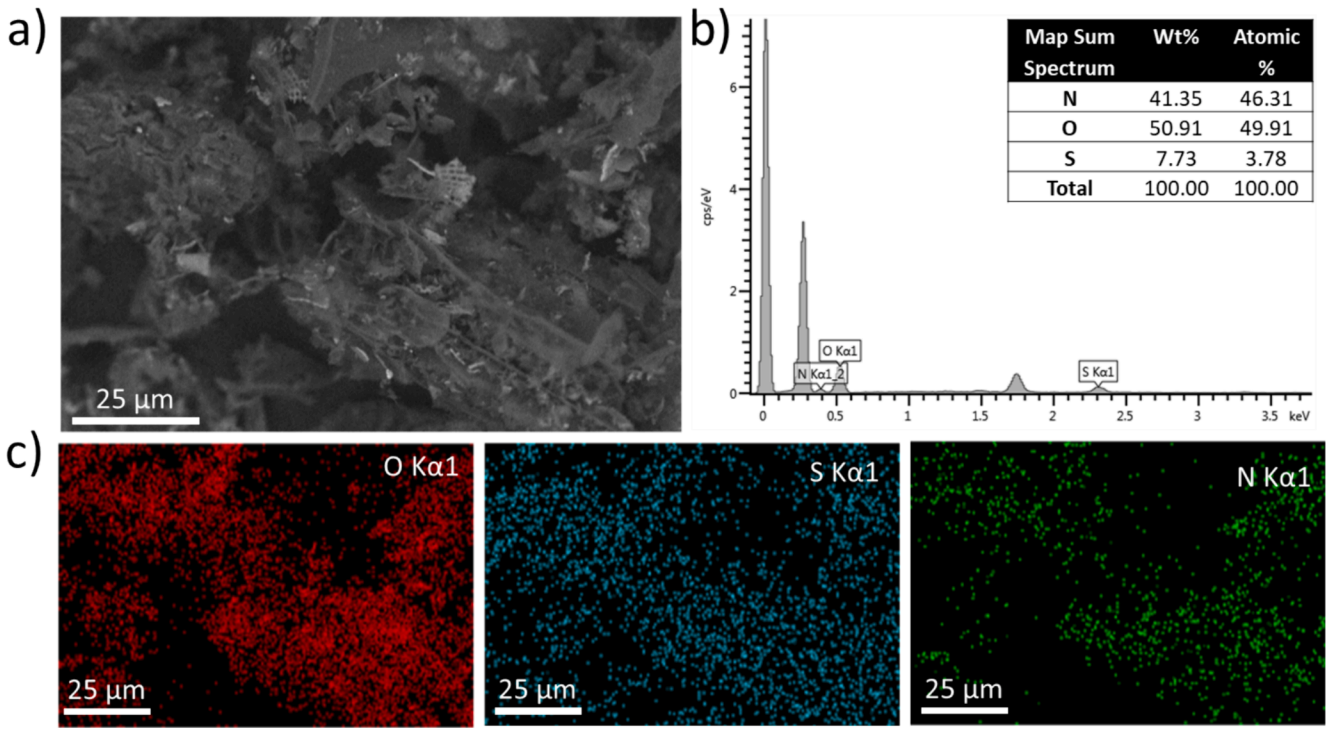

Fig.2. (a) SEM images of ABS. (b) EDX spectrum and compositional analysis (inset table), and (c) the corresponding element maps of O, S, and N measured for ABS.

The concentrated electronic states respond more efficiently to changes in electrostatic potential, enhancing the material's ability to store electrical charge. This heightened quantum capacitance is advantageous for applications such as SCs, in which rapid and responsive charge storage is crucial [58].

In contrast, undoped counterparts lack the specific configurations that introduce these localized states, resulting in less favorable electronic properties and a comparatively lower quantum capacitance [57,59]. The concomitant presence of N and O is associated with the presence of defects and redox active sites in carbonaceous active materials. Additionally, carbon atoms can function as Lewis bases by donating electron pairs. The redox-active sites are typically associated with the carbon atoms adjacent to pyridinic N, rather than the pyridinic N atoms themselves [60]. Like pyridinic N, sulfate S exhibits electron-deficient characteristics, thereby promoting the formation of redox-active sites involving conjoint carbon atoms for ion storage processes. In contrast, thiophene is considered an electron-rich system with a weak ability to accept electrons [61]. Consequently, the carbon atoms neighboring pyridinic N and sulfate S, possessing Lewis basicity, may play a crucial role in enhancing electron transport and facilitating ion diffusion in SC electrodes [60]. Also, the surface activated biochar is enriched with O, resulting in tunable hydrophilicity, regulating the wetting behavior and ion transport [39]. In general, redox-active defective carbon sites can be transformed into ether or carbonyl groups that also exhibit limited reactivity towards electrolyte decomposition reactions [62].

2.1. Electrochemical characterization

The ABS presented in this work has a unique structure of a three-dimensional carbon skeleton with a large surface area of up to 821 m^2g^{-1} and hierarchical porosity combining micropores and mesopores. These properties make the ABS a suitable active material for high-capacitance SC electrodes. In addition, the interplay between electrode materials and electrolytes must be considered when designing high-energy density SCs. In fact, the overall electrode capacitance depends on the electrolyte ion accessibility to the surface of active materials. Meanwhile, the SC energy density increases with the electrochemical stability window (ESW) of the electrolyte, whose reactivity is, in turn, influenced by the electrode materials in contact with itself [63]. Different types of electrolytes, including aqueous electrolytes, organic electrolytes, ionic liquids, and solid/quasi-solid-state electrolytes, have been proposed for SCs, each with its advantages and disadvantages [64,65]. Aqueous electrolytes have advantages in terms of high ionic conductivity and environmental friendliness compared with organic ones. However, their ESW is severely restricted by the oxygen evolution reaction (OER) and hydrogen evolution reaction (HER) [66,67], thus limiting Es, as well as stability under accelerated aging tests (*e.g.*, voltage floating) [68]. Nevertheless, the formation of hydrated solid phases or highly viscous aqueous solutions in highly concentrated electrolytes can slow down the occurrence of irreversible water splitting reactions because of the reduced availability of free-water molecules near the electrode surface [66,69]. Also, the low catalytic activity of carbonaceous materials in near-neutral pH electrolytes (*e.g.*, $NaNO_3$ and other nitrates) [66], attributed to the local acidification and basification at surfaces of the positive and negative electrode, respectively, is an effective strategy to extend the device ESW beyond the thermodynamic voltage of water splitting (*i.e.,* 1.23 V), even up to more than 2 V [66,69,70]. Of course, traditional organic electrolytes, such as $TEABF_4$/ACN and $TEABF_4$/polycarbonate (PC), represent the robust benchmark enabling SC operation up to voltage between 2.4–2.7 V, leading to Es typically between 15–30 Wh kg^{-1}, depending on the active material specifications [71]. Nonetheless, aqueous electrolytes still represent a cost-effective solution (price of $NaNO_3$ is $< 0.2\ \$\ g^{-1}$, *versus ca.* 14.7 $\$\ g^{-1}$ for $TEABF_4$) [72,73], showing interesting properties in terms of ion conductivity (ranging from 10 to 100 mS cm^{-1}) [72] and ion size (smaller than organic electrolyte ions) that ensure high-power density and high capacitance performances, respectively [71]. Furthermore, SSEs have been developed to compensate limitations associated with liquid electrolytes, including electrolyte leakage and excess weight. In this context, polymeric SSEs provide outstanding mechanical stability, including bendability and foldability, and eliminate concerns associated with leakage, flammability, and corrosivity of organic electrolytes. These advantages, coupled with the potential for a

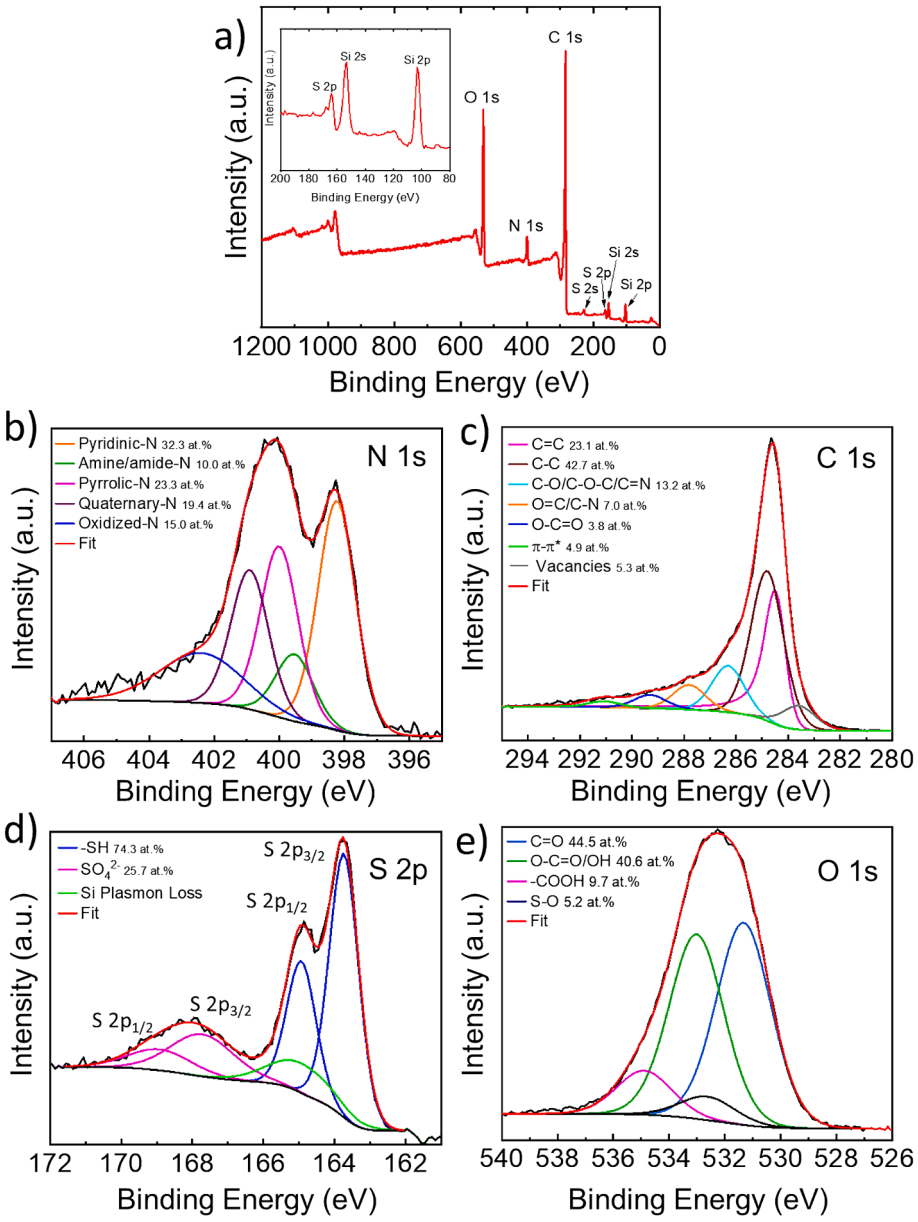

Fig.3. (a) Wide scan XPS spectrum of the ABS. (b) N 1s, (c) C 1s, (d) S 2p, and (e) O 1s XPS spectra of the ABS.

more compact and denser design, make SSEs particularly suitable for various applications in portable and wearable electronics, including biomedical implants and health monitoring devices.

Based on these considerations, the ABS was evaluated as an active material for electrodes for EDLC-type SCs based on representative aqueous and organic electrolytes, namely 1 M H_2SO_4 (acid) and 8 M $NaNO_3$ (near-neutral) aqueous electrolytes and 1 M $TEABF_4$/ACN, organic electrolyte. Also, taking advantage of our previous work [34], the performance of the ABS active materials was investigated in the presence of a SSE made of a SPEEK:f-NbS_2 composite membrane activated in 1 M H_2SO_4 and 8 M $NaNO_3$ solutions. In addition, as an alternative to polyvinylidene fluoride (PVDF) binder, SPEEK was screened as

Table 2
List of the investigated SC configurations and the AC-based EDLC (reference devices) using different electrolytes and binders including relevant performance metrics.

Active material	Binder	Separator/SSE	Electrolyte	Acronym	WVW (V)	C_g (Fg^{-1})	Es ($Wh\ kg^{-1}$)
ABS	SPEEK	Glassy fiber (gf)	1 M H_2SO_4	ABS-H_2SO_4	1	109.5	3.4
ABS	SPEEK	gf	8 M $NaNO_3$	ABS-$NaNO_3$	1.6	79.0	6.3
ABS	PVDF	gf	1 M $TEABF_4$/ACN	ABS-$TEABF_4$	2.4	64.3	12.4
ABS	SPEEK	SPEEK:f-NbS_2	SSSC-H_2SO_4	1	100.6	3.1	
ABS	SPEEK	SPEEK:f-NbS_2	SSSC-$NaNO_3$	1.6	66.7	5.4	
AC	SPEEK	gf	1 M H_2SO_4	AC-H_2SO_4 (ref.)	1	124.5	3.7
AC	SPEEK	gf	8 M $NaNO_3$	AC-$NaNO_3$ (ref.)	1.6	88.1	6.8
AC	PVDF	gf	1 M $TEABF_4$/ACN	AC-$TEABF_4$ (ref.)	2.4	71.4	14.8

an ion-exchange polymeric binder in the presence of aqueous electrolytes and SSE. The performances of ABS were also compared to those of a commercially available AC. Table 2 lists the details of the investigated SC configurations, including their nomenclatures and indicating the working voltage window (WVW) used to measure their performances.

Fig. 4a shows the cyclic voltammetry (CV) curves measured for the ABS-based SCs, *i.e.,* ABS-H_2SO_4, ABS-$NaNO_3$, and ABS-$TEABF_4$ at voltage scan rate of 100 mV/s and using WVWs of 1.0, 1.6, and 2.4 V, respectively. The shapes of the CV curves are nearly rectangular, indicating capacitive behavior. Fig. S4a-c illustrates CV curves measured for ABS-H_2SO_4, ABS-$NaNO_3$, and ABS-$TEABF_4$ electrodes at various voltage scan rates, ranging from 5 to 1500 mVs^{-1}. The SC curves maintained their quasi-rectangular shape with the increase of the voltage scan rate, indicating satisfactory rate capability. Fig. 4b shows the galvanostatic charge–discharge (GCD) analysis of the ABS-H_2SO_4, ABS-$NaNO_3$, and ABS-$TEABF_4$ electrodes at 0.5 Ag^{-1}. The triangular GCD profiles confirm the capacitive behavior of these devices. Fig. S4a-c reports the GCD profiles recorded for these devices at various specific currents, ranging from 0.1 to 50 Ag^{-1}, evidencing almost ideal capacitive behaviors, thus, confirming CV results. Furthermore, CV and GCD analyses were performed on SCs based on commercial AC as the active material, *i.e.,* AC-H_2SO_4 (ref.), AC-$NaNO_3$ (ref.), and AC-$TEABF_4$ (ref.), (Fig. S5a-c). Compared to ABS-based SCs, the specific currents and time discharges are similar. Fig. 4c shows the electrode C_g measured for the ABS-based SCs as a function of the specific current. At 0.1 Ag^{-1}, ABS-H_2SO_4, ABS-$NaNO_3$, and ABS-$TEABF_4$ EDLCs achieved electrode C_g of 109.5, 79.0 and 64.3Fg^{-1}, respectively.

By increasing the specific current to 50 Ag^{-1}, the C_g decreased to 78.6, 52.9, and 40.5 Fg^{-1}, for ABS-H_2SO_4, ABS-$NaNO_3$, and ABS-$TEABF_4$ EDLCs, respectively. This reduction is a consequence of ohmic losses, including those associated with the ion diffusion within the pores of the ABS [74]. Amongst the SC configurations, the differences in C_g can be attributed to the ionic radius and conductivity of the electrolytes [75]. Table S4 reports the ionic and solvation sphere values for different ions, revealing a trend for the solvated ion size: $H^+ < Na^+ < TEA^+$. Notably, H^+ ions exhibit the highest molar ionic conductivity, while TEA^+ ions show the lowest one. Additionally, SO_4^{2-} ions exhibit a molar ionic conductivity higher than that of BF_4^- ions [76]. According to the molecular ionic conductivities, 1 M $TEABF_4$/ACN shows ionic conductivity in the range of 50–60 mS cm^{-1} (*e.g.,* 52.1 [77], and 60.0 [78] mS cm^{-1}), while 8 M $NaNO_3$ and 1 M H_2SO_4 exhibit higher ionic conductivity, *e.g.*, ~170 [69] and ~ 800 mS cm^{-1} [79], respectively. In our ABS-based

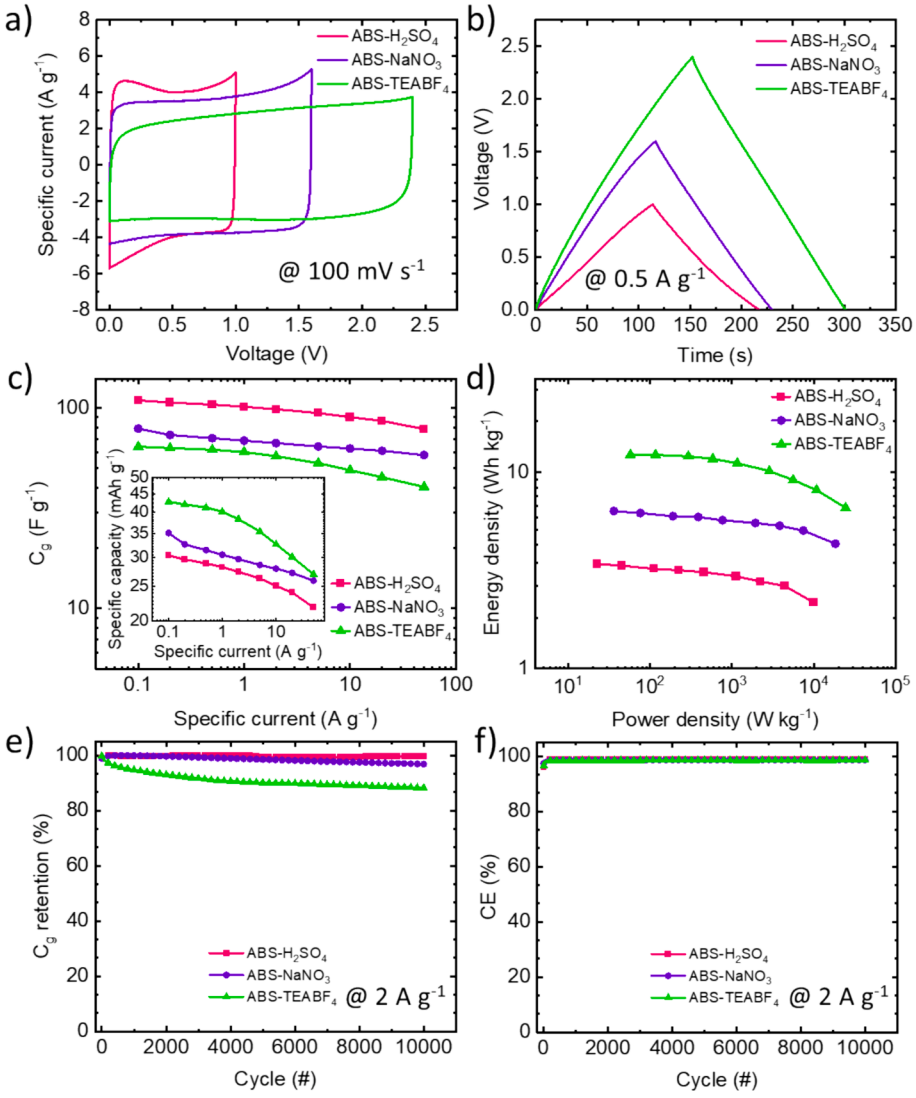

Fig.4. Electrochemical characterization of the investigated ABS-based SCs in different electrolytes. (a) CV curves, measured at 100 mVs^{-1}, and (b) GCD profiles, measured at 0.5 Ag^{-1}, for ABS-H_2SO_4, ABS-$NaNO_3$, and ABS-$TEABF_4$ SCs. (c) Electrode C_g (inset, specific capacity) measured for the investigated ABS-based EDLCs as a function of the specific current (data extrapolated from the GCD profiles). (d) Ragone plots, (e) C_g retention, and (f) CE over 10,000 GCD cycles at 2 Ag^{-1} measured for the investigated ABS-based SCs.

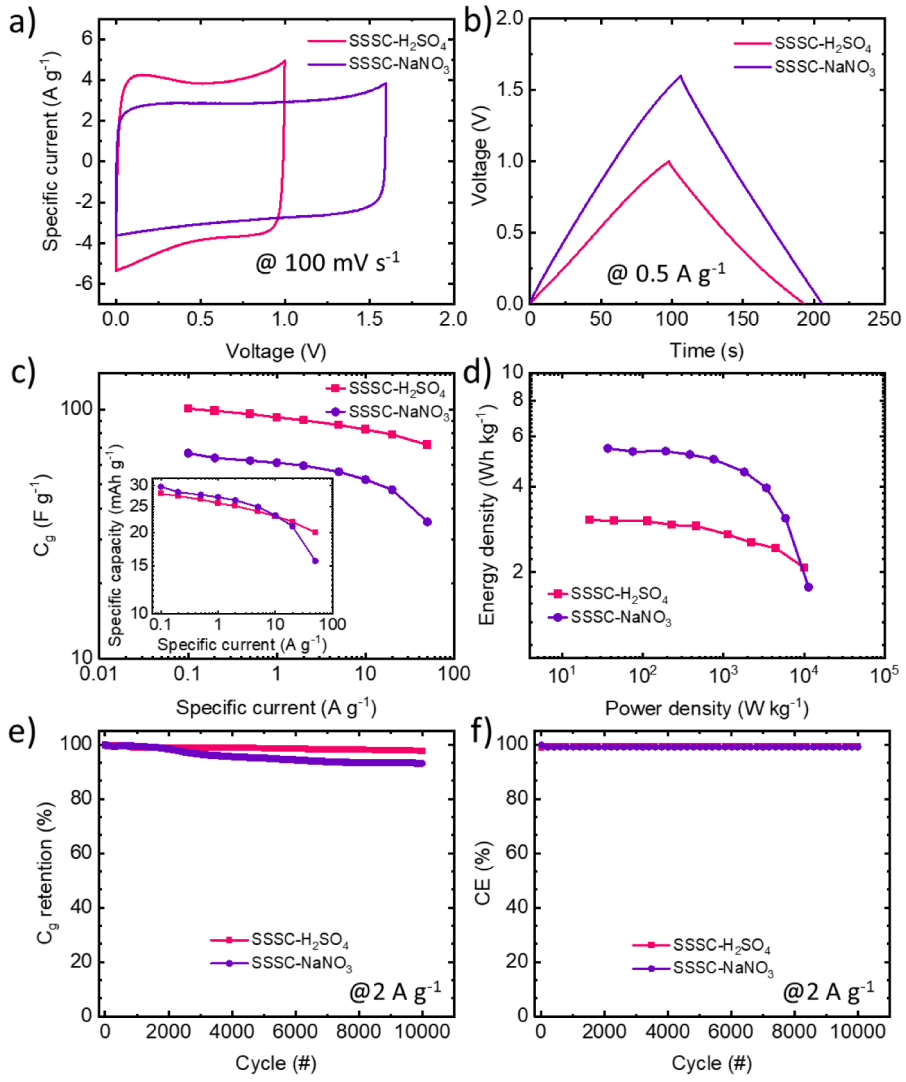

Fig.5. Electrochemical characterization of the investigated SSSCs. (a) CV curves, measured at 100 mV/s, (b) GCD profiles, measured at 0.5 Ag^{-1}, for SSSC-H_2SO_4 and SSSC-$NaNO_3$ SCs. (c) Electrode C_g (inset, specific capacity) measured for the investigated SSSCs as a function of the specific current (data extrapolated from the GCD analysis). (d) Ragone plots, (e) C_g retention, and (f) CE over 10,000 GCD cycles at 2 Ag^{-1} measured for the investigated SSSCs.

electrodes, the interplay between ion size and mobility can significantly affect the overall capacitive performance. Differently from the ABS-$TEABF_4$/ACN, the micropores in ABS-H_2SO_4 and ABS-$NaNO_3$ electrodes can efficiently accommodate solvated ions, leading to outstanding C_g, especially for the 1 M H_2SO_4 electrolyte. The superior C_g of aqueous SCs compared to counterpart based on organic electrolytes is a commonly observed behavior [80]. Compared to aqueous AC-based SCs, the superior capacitive performance of the ABS-based SCs is attributed to their key structural characteristics. The porous structure facilitates efficient charge and ion transport even into micropores, while mesopores act as ion-buffering reservoirs [81,82]. The presence of heteroatom functional groups within ABS provides additional sites for charge storage and promotes redox reactions, introducing a pseudocapacitance contribution [83]. The electrode C_g (and specific capacities) measured for reference AC-based SCs are reported in Fig. S6. Regarding the specific capacity (Fig. 4c, inset), ABS-$TEABF_4$ outperforms ABS-H_2SO_4, and ABS-$NaNO_3$, since the former was evaluated in a larger WVW (*i.e.,* 2.4 V). As shown in Fig. S7a and b, the Coulombic efficiency (CE) of the investigated SCs is almost 100% at high specific currents, *i.e.,* >5 Ag^{-1}. At lower current density, CE progressively decreases as a consequence of parasitic reactions, which are more pronounced in the presence of aqueous electrolytes, in particular in 1 M H_2SO_4 [66]. The energy efficiency (EE) remains in the range of 70 to 90% and exhibits a peak at moderate specific currents (from 1 to 2 Ag^{-1}), reflecting efficient charge storage without relevant ohmic losses associated with internal series resistances, which is higher in ABS-$TEABF_4$ [84]. The CE and EE measured for the AC-based devices are reported in Fig. S8a-b, and their trends are similar to those of ABS-based SCs.

Electrochemical impedance spectroscopy (EIS) was carried out to evaluate the capacitive, resistive, and charge transport characteristics of the investigated devices. As shown in Fig. S9, the Nyquist plots in the low-frequency region display nearly vertical straight lines, which are indications of a capacitive behavior. The slope deviation from 90° is associated with ion diffusion into electrode material pore channels, as modeled by the so-called Warburg impedance (W) [85]. The intercept at high frequency provides information on bulk electrolyte resistance (R_e), decreasing in the order of $TEABF_4$ > $NaNO_3$ > H_2SO_4. These trends are consistent with the one of the ionic conductivities of the electrolytes. The R_e values measured for ABS-H_2SO_4, ABS-$NaNO_3$, and ABS-$TEABF_4$ electrodes are 0.43, 0.66, and 0.87 Ω, respectively. The small semicircle in the high/frequency region of the Nyquist plot represents the RC circuit given by the current collector/electrode interface[13], even though it may include the impedance contribution associated with parasitic redox reactions. The semicircle diameter denotes an overall charge

transfer resistance (R_{ct}) [86], which decreases in the order of ABS-H_2SO_4 < ABS-$NaNO_3$ < ABS-$TEABF_4$. This behavior is likely associated with the presence of parasitic water splitting reactions, which are more pronounced in acid aqueous electrolytes compared to the other cases, as discussed in ref. [66].

Fig. 4d displays the Ragone plot (*i.e.,* Es *vs.* Ps) of the ABS-based SCs, as derived from their GCD analysis. As expected by its largest WVW, ABS-$TEABF_4$ exhibited the highest Es, achieving 12.4 Wh kg^{-1} at 57.4 W kg^{-1} and 24.5 kW kg^{-1} at 6.6 Wh kg^{-1}. In the neutral and acidic aqueous electrolytes, the devices reached Es of 6.3 Wh kg^{-1} at 36.1 W kg^{-1} and 3.4 Wh kg^{-1} at 22.5 W kg^{-1}, respectively. Fig. S10 shows the Ragone plots measured for the AC-based SCs. The AC-H_2SO_4 (ref.), AC-$NaNO_3$ (ref.), and AC-$TEABF_4$ (ref.) achieved Es of 3.7 Wh kg^{-1} at 21.7 W kg^{-1}, 6.8 Wh kg^{-1} at 34.8 W kg^{-1}, and 14.8 Wh kg^{-1} at 62.2 W kg^{-1}, respectively. Furthermore, equivalent series resistance (ESR) and maximum specific power (P_{max}), were calculated according to equations S6 and S7. The calculated ESR values are 1.3, 1.0, and 0.61 Ω for ABS-$TEABF_4$, ABS-$NaNO_3$ and ABS-H_2SO_4, respectively. These ESR values correspond to P_{max} of 378, 222, and 147 kW kg^{-1}, respectively. Noteworthy, ESR depends on the electrolyte ionic conductivity as well as by other resistance contribution associated with either transport of the electrolyte within the porous electrodes or current collector/electrode film interfaces. Meanwhile, P_{max} is inversely proportional to the ESR but is also proportional to the square of the WVW. Consequently, even though ABS-$TEABF_4$ exhibits the highest ESR amongst the investigated devices with liquid electrolyte (see Fig. S9 and Table S4**),** it achieves the highest P_{max} (378 kW kg^{-1}) owing to its larger WVW (*i.e.,* 2.4 V). Despite the ABS-H_2SO_4 exhibits the lowest ESR (0.61 Ω), its limited WVW (1 V) also leads to the lowest P_{max} of 147 kW kg^{-1}.

In general, ABS and AC resulted in similar performances, regardless of electrolytes. Nevertheless, thanks to the sustainability of its precursors, ABS may represent a sustainable alternative to common ACs produced from non-renewable resources. The long-term cyclic stability of ABS-based SCs was assessed over 10,000 GCD cycles at a current density of 2 Ag^{-1}. As shown in Fig. 4e**,** the cyclic stability of aqueous SCs surpassed that obtained with organic electrolytes. Particularly, ABS-H_2SO_4 retained 99.6% of its C_g. In contrast, ABS-$TEABF_4$ exhibited a C_g retention of 88%. Nevertheless, strategies, for example, concerning the optimization of the electrode mass ratio can be prospectively used to minimize the degradation rate of devices based on organic electrolytes [87]. The investigated devices maintained a CE exceeding 98% at the end of the stability test (Fig. 4f), indicating satisfactory reversibility over cycling. Table S5 compares the performance of ABS-based SCs with those obtained with biomass/derived active materials reported in the literature.

Furthermore, Fig. 5 shows the results obtained for SSSC-H_2SO_4, and SSSC-$NaNO_3$ solid-state SCs (SSSCs), assembled with the SPEEK:f-NbS_2 composite membranes (activated in 1 M H_2SO_4 and 8 M $NaNO_3$, respectively) as SSEs. Fig. 5a reports the CV curves measured for SSSC-H_2SO_4 and SSSC-$NaNO_3$ at the voltage scan rate of 100 mVs^{-1}, indicating the capacitive behavior of the devices, as also associated with the effective ion transport of the SSEs. Compared to the SSSC-$NaNO_3$ case, the higher specific currents measured for SSSC-H_2SO_4 reflects the superior H^+ conductivity compared to Na^+ in ion-exchanging polymeric membranes [88,89]. Fig. 5b shows the GCD analysis for both devices at a specific current of 0.5 Ag^{-1}, confirming a nearly capacitive behavior. The CV data acquired for the SSCs at various voltage scan rates, ranging from 5 to 1500 mVs^{-1}, are shown in Fig. S11a-b. By increasing the voltage scan rate in SSSC-$NaNO_3$, a slight deformation of the rectangular CV shape suggests an inferior rate capability compared to that of SSSC-H_2SO_4 [82].

Fig. S11c-d depict the GCD profiles measured for SSSC-H_2SO_4 and SSSC-$NaNO_3$ at various specific currents, ranging from 0.1 to 50 A g^{-1}. These data confirm the superior rate capability of SSSC-H_2SO_4 compared to SSSC-$NaNO_3$, because of the different ion transport abilities of the SSEs. In our specific SSEs, the ion transport ability results from the interactions of sulfuric acid functional groups in polymeric chains and f-$SNbS_2$ nanosheets with cations (*i.e.*, H^+ and Na^+) [90]. Thus, in SSSC-H_2SO_4, sulfuric acid groups enhance H^+ ion transport, benefiting from their small size and high mobility, leading to excellent ion conductivity (*i.e.*, ~94 mS cm^{-1}) [34]. Fig. 5c displays the C_g and specific capacity measured for SSSC-H_2SO_4 and SSSC-$NaNO_3$ as a function of the specific current, from 0.1 to 50 A g^{-1}. The C_g decreases from 100.6Fg^{-1} to 74.9Fg^{-1} for SSSC-H_2SO_4 (74.4% C_g retention) and from 66.7Fg^{-1} to 35.3Fg^{-1} for SSSC-$NaNO_3$ (53.2% C_g retention) as the specific current increases from 0.1 to 50 A g^{-1}, remarking the excellent rate capability of SSSC-H_2SO_4. Fig. S12a-b illustrates the CE and EE obtained for SSSC-H_2SO_4 and SSSC-$NaNO_3$ as a function of the specific current. SSSC-$NaNO_3$ shows a CE of 79% at 0.1 A g^{-1}, indicating the presence of current leakage at the electrode–electrolyte interface due to parasitic electrochemical reactions. The latter may be reduced by lowering the WVW to less than 1.4 V. In this case, the insufficient Na^+ transport in SSE may also results in a poor balance of the electrode capacities, limiting the WVW to lower values compared to the aqueous SC based on 8 M $NaNO_3$. Conversely, at 0.1 A g^{-1}, SSSC-H_2SO_4 still exhibited a CE as high as 93%, indicating the possibility of reducing parasitic reaction compared to the aqueous SC using 1 M H_2SO_4 electrolyte [91]. In terms of EE, SSSC-H_2SO_4 outperformed SSSC-$NaNO_3$ and reached EEs of 75.8% and 63.2% at 0.1 and 50 A g^{-1}, respectively. Fig. S13 shows the EIS analysis of SSSCs, indicating that SSSC-H_2SO_4 has an R_s value of 0.78 Ω, lower than the one of SSSC-$NaNO_3$ (1.0 Ω). Also, SSSC-$NaNO_3$ exhibited a R_{ct} of 1.9 Ω, which is higher than the one of SSSC-H_2SO_4 (0.34 Ω), in agreement with the EE trends of these devices. Fig. 5d presents the Ragone plots of the SSSCs, showing that SSSC-H_2SO_4 achieved a maximum Es of 3.1 Wh kg^{-1} at 21.8 W kg^{-1} and a maximum Ps of 10 kW kg^{-1} at 2.1 Wh kg^{-1}, while SSSC-$NaNO_3$ reached a maximum Es of 5.4 Wh kg^{-1} at 36.7 W kg^{-1} and a maximum Ps of 11.3 kW kg^{-1} at 1.8 Wh kg^{-1}.

SSSC-$NaNO_3$ exhibits higher P_{max} (88 kW kg^{-1}) despite its higher ESR (2.6 Ω) than SSSC-H_2SO_4 (P_{max} of 54 kW kg^{-1} and ESR of 1.6 Ω). Additionally, Fig. 5e-f reveal the cyclic stability of SSSC-H_2SO_4 and SSSC-$NaNO_3$. After 10,000 GCD cycles at 2 A/g, SSSC-H_2SO_4 retained 96.7% and 99.0% of its C_g and CE, respectively. These results emphasize the excellent cyclability of SSSC-H_2SO_4, superior to that of its aqueous analogous. Fig. S14 shows the Raman analysis of ABS-based electrodes after 10,000 GCD cycles to evaluate the impact of electrolytes and the GCD cycling on their structure. In fact, the analysis of the I_D/I_G ratio can reflect the evolution of the structural characteristics of the electrodes before and after cyclic stability analysis [27,92]. As shown in Fig. S14b, the pristine electrode exhibits an initial I_D/I_G ratio of approximately 0.88. For all the samples except ABS-$TEABF_4$, the I_D/I_G ratio has shown non-relevant changes after 10,000 GCD cycles, indicating that the electrodes maintained their structural and morphological integrity during cycling. In contrast, ABS-$TEABF_4$ undergoes substantial structural changes, likely explaining the C_g fade during GCD cycling (see Fig. S4c).

Table 2 provides a comparison between C_g and Es measured for the investigated devices. Also, Fig. 6a-b serves as a visual (qualitative) aid for comparing the performances (expressed in scorecards) of the ABS-based SCs, distinguished on the basis of their electrolyte, covering five key metrics: C_g, specific capacity, maximum achieved Es, P_{max}, and cyclic stability after 10,000 GCD cycles. These key parameters are categorized into five levels (ranging from 1 to 5), with higher values signifying a more favorable impact of the electrolytes on the performance metrics of ABS-based SCs. The H_2SO_4-based results in better C_g than other samples due to the small size of solvated H^+. Conversely, $TEABF_4$/ACN limits the C_g due to the large size of its solvated ions (TEA^+ and BF_4^-), impeding effective access into the microporosities of the ABS. In terms of Es, $TEABF_4$/ACN and $NaNO_3$-based electrolytes provide clear benefits thanks to their larger WVW compared to that of H_2SO_4-based electrolytes. Cycling stability is given by aqueous electrolytes, particularly H_2SO_4-based ones, while $TEABF_4$/ACN may cause mechanical

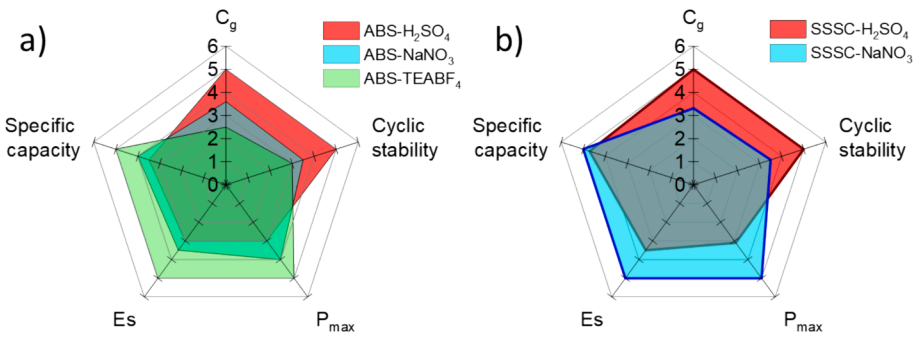

Fig.6. Comparative analysis, qualitatively expressed in form of scorecards, of the key metrics of SCs based on (a) liquid electrolytes, *i.e.,* 1 M H_2SO_4, 8 M $NaNO_3$, and 1 M $TEABF_4$/ACN and (b) SSEs.

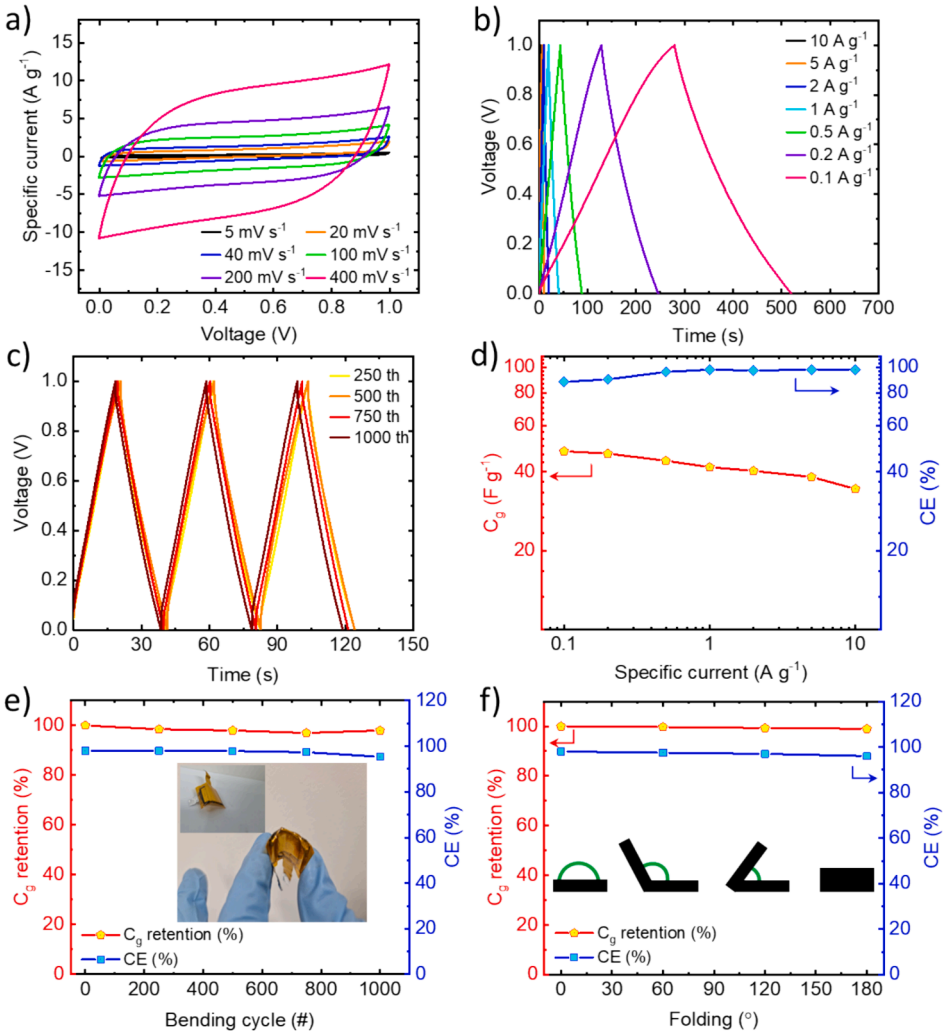

Fig.7. Electrochemical characterization of the ABS-based FSSSC. (a) CV curves measured at different voltage scan rates, ranging from 5 to 400 mVs^{-1}, (b) GCD profiles measured at various specific currents, ranging from 0.1 to 10 Ag^{-1}. (C) C_g and CE as function of the specific current. (d) GCD profiles measured after 250, 500, 750, and 1000 bending cycles at 1 Ag^{-1} (curvature radius = 2 cm). (e) C_g retention and CE of the FSSSC over 1000 bending cycles. (f) C_g retention and CE of the FSSSC folded at 0°, 60°, 120°, and 180°.

stresses associated with the large size of its solvated ions. Furthermore, ABS-$TEABF_4$ SC exhibits the highest P_{max} despite its highest ESR, emphasizing the dominant effect of the WVW on the performance of the SCs. Fig. 6b shows the scorecards assigned to SSSCs. Compared to SSSC-$NaNO_3$, SSSC-H_2SO_4 offers higher C_g and cyclic stability but lower P_{max} and Es.

To fulfill practical demands, ABS-based FSSSC were assembled and characterized upon applying mechanical stresses. Based on the previous electrochemical characterization, SSSC-H_2SO_4 was selected to assemble our FSSSC, as depicted in Fig. 7. The active area of the device was 1.2 cm × 1.6 cm, obtained by sandwiching a SPEEK-2.5%-f-NbS_2:SPEEK composite SSE, activated in 1 M H_2SO_4, between two ABS-based electrodes deposited on flexible carbon cloths, serving as current collectors. Fig. 7a reports the CV curves measured for the FSSSC at various voltage scan

rates, ranging from 5 to 400 mVs^{-1}. The rectangular shape of the CV curves indicates the capacitive behavior of the device, as also confirmed by the triangular shape of its GCD profiles (Fig. 7b**)**. As shown in Fig. 7c, the FSSSC exhibited a satisfactory rate capability, retaining 72% of its C_g measured at 0.1 Ag^{-1} when tested at the highest specific current of 10 Ag^{-1}. After subsequent bending cycles (250, 500, 750, and 1000) at 1 Ag^{-1}, the FSSSC optimally retained its C_g and CE (Fig. 7d). In particular, the FSSSC retained 97 % of C_g and 98 % of CE after 1000 bending cycles at a curvature radius of 2 cm (Fig. 7e), demonstrating remarkable flexibility. The performances of the device were also examined under 60°, 120°, and 180° folding angles, demonstrating excellent folding resistance. As shown in Fig. 7**f,** the FSSSC retained >95 % of its C_g for all the folding conditions. The remarkable mechanical stability of the FSSSC during bending and folding is attributed to the unique mechanical properties of the optimized composite SSE, 2.5%-f-NbS_2:SPEEK, the mechanical robustness of the ABS-based electrodes and the flexibility of carbon cloth current collectors.

3. Conclusion

This study has successfully demonstrated a sustainable and high-performance electrode active material for supercapacitors (SCs) derived from Venice lagoon's Sargassum brown macroalgae. A self-doped porous activated biochar (ABS) was produced exploiting a straightforward thermochemical process, followed by CO_2 activation. The electrochemical characterization of ABS-based SCs in various electrolytes, including aqueous (1 M H_2SO_4, and 8 M $NaNO_3$), organic (1 M $TEABF_4$/ACN), and solid-state electrolytes (SSEs) sulfonated poly ether ether ketone:functionalized niobium disulfide flakes (SPEEK: f-NbS_2) composites, demonstrates promising capacitive performances in terms of C_g, energy/power densities, efficiency, and cyclic stability. With liquid electrolytes, ABS-based SCs achieved energy densities of 3.4 Wh kg^{-1} at 22.5 W kg^{-1}, 6.3 Wh kg^{-1} at 36.1 W kg^{-1}, and 12.4 Wh kg^{-1} at 57.4 W kg^{-1}, and maximum power densities of 147, 222, and 378 kW kg^{-1}, in the acidic, quasi-neutral aqueous electrolyte and organic electrolyte, respectively. Furthermore, after evaluating the electrochemical performance of the ABS-based electrodes in solid-state supercapacitor, a flexible solid-state supercapacitor (FSSSC) was fabricated based on ABS-electrode and SPEEK:f-NbS_2 SSE. Our FSSSC stably operated under mechanical stress, including bending up to 1000 times and folding angles up to 180°, retaining more than 95% of its initial C_g. The outstanding performance of ABS-based SCs is attributed to its pore distribution, heteroatom doping, and improved surface characteristics. These features synergistically create abundant active sites for charge accumulation, promote effective electrolyte diffusion, and elevate electrochemical activity. These findings highlight the considerable potential of ABS as an environmentally friendly and high-performance alternative to conventional activated carbon for SCs and other energy storage applications.

4. Experimental section

Detailed information related to the preparation of activated biochar derived from Sargassum, electrodes and electrolytes preparation, physicochemical characterization, and electrochemical evaluation of ABS-based electrodes for supercapacitor application is provided in Supporting Information.

The authors declare that they have no known competing financial interests or personal relationships that could have appeared to influence the work reported in this paper. A. Bagheri, S. Bellani, H. Beydaghi, J-K. Panda, M. I. Zappia, V. Mastronardi, A. Gamberini, S. B. Thorat, M. Abruzzese, and F. Bonaccorso are employees of BeDimensional S.p.A., a company producing two-dimensional materials.

CRediT authorship contribution statement

Ahmad Bagheri: Writing – original draft, Methodology, Investigation, Conceptualization. **Somayeh Taghavi:** Methodology, Investigation, Data curation. **Sebastiano Bellani:** Writing – original draft, Methodology, Investigation, Formal analysis, Data curation, Conceptualization. **Pejman Salimi:** Methodology, Investigation, Data curation. **Hossein Beydaghi:** Methodology, Investigation. **Jaya-Kumar Panda:** Methodology, Investigation. **Marilena Isabella Zappia:** Methodology, Investigation. **Valentina Mastronardi:** Methodology, Investigation. **Agnese Gamberini:** Methodology, Investigation, Data curation. **Sanjay Balkrishna Thorat:** Methodology. **Matteo Abruzzese:** Methodology, Investigation. **Lea Pasquale:** Methodology, Data curation. **Mirko Prato:** Methodology, Data curation. **Michela Signoretto:** Methodology, Investigation, Data curation. **Xinliang Feng:** Writing – review & editing, Methodology, Funding acquisition. **Francesco Bonaccorso:** Writing – review & editing, Supervision, Resources, Investigation, Conceptualization.

Declaration of competing interest

The authors declare the following financial interests/personal relationships which may be considered as potential competing interests: [The authors declare the following financial interests/personal relationships which may be considered as potential competing interests: Francesco Bonaccorso reports financial support was provided by BeDimensional S.p.A. Francesco Bonaccorso reports a relationship with BeDimensional S.p.A. that includes: board membership. None If there are other authors, they declare that they have no known competing financial interests or personal relationships that could have appeared to influence the work reported in this paper].

Data availability

Data will be made available on request.

Acknowledgments

This project has received funding from the European Union's Horizon 2020 research and innovation program under the Marie Skłodowska-Curie Grant Agreement No. 813036, the European Union's GREENCAP Horizon Europe research and innovation program under Grant Agreement No. 101091572, 2D-PRINTABLE Horizon Europe research and innovation program under Grant Agreement No. 694101, the European Union's Horizon 2020 research and innovation program under Grant Agreement No. 881603-GrapheneCore3, and the European Union's SENSIBAT project under Grant Agreement No. 957273. We thank the Electron Microscopy and Material Characterization facilities-Istituto Italiano di Tecnologia- for support in SEM/TEM, XPS and XRD data acquisition, respectively.

Appendix A. Supplementary data

Supplementary data to this article can be found online at https://doi.org/10.1016/j.cej.2024.153529.

References

[1] D. Spurling, H. Krüger, N. Kohlmann, F. Rasch, M.P. Kremer, L. Kienle, R. Adelung, V. Nicolosi, F. Schütt, 3D networked MXene thin films for high performance supercapacitors, Energy Storage Mater. 65 (2024) 103148.
[2] A. Bagheri, M. Javanbakht, H. Beydaghi, P. Salarizadeh, A. Shabanikia, H., Salar Amoli, Sulfonated poly(etheretherketone) and sulfonated polyvinylidene fluoride-co-hexafluoropropylene based blend proton exchange membranes for direct methanol fuel cell applications, RSC Adv. 6 (2016) 39500–39510.
[3] Y. Xie, M. Li, R. Huang, N. Cao, D. Chao, How much of the energy in the electrochromic energy storage window can be reused? Energy Storage Mater. 67 (2024) 103321.

[4] S.N. Banitaba, S.V. Ebadi, P. Salimi, A. Bagheri, A. Gupta, W.U. Arifeen, V. Chaudhary, Y.K. Mishra, A. Kaushik, E. Mostafavi, Biopolymer-based electrospun fibers in electrochemical devices: versatile platform for energy, environment, and health monitoring, Mater. Horizons 9 (2022) 2914–2948.

[5] E. Pomerantseva, F. Bonaccorso, X. Feng, Y. Cui, Y. Gogotsi, Energy storage: The future enabled by nanomaterials, Science 366 (2019) eaan8285.

[6] F. Bonaccorso, L. Colombo, G. Yu, M. Stoller, V. Tozzini, A.C. Ferrari, R.S. Ruoff, V. Pellegrini, Graphene, related two-dimensional crystals, and hybrid systems for energy conversion and storage, Science 347 (2015) 1246501.

[7] M.S. Alam, A.A. Almehizia, F.S. Al-Ismail, M.A. Hossain, M.A. Islam, M. Shafiullah, A. Ullah, Frequency Stabilization of AC Microgrid Clusters: An Efficient Fractional Order Supercapacitor Controller Approach, Energies 15 (2022) 5179.

[8] S. Zheng, Z.S. Wu, S. Wang, H. Xiao, F. Zhou, C. Sun, X. Bao, H.M. Cheng, Graphene-based materials for high-voltage and high-energy asymmetric supercapacitors, Energy Storage Mater. 6 (2017) 70–97.

[9] K.C.S. Lakshmi, B. Vedhanarayanan, High-Performance Supercapacitors: A Comprehensive Review on Paradigm Shift of Conventional Energy Storage Devices, Batteries 9 (2023) 202.

[10] P. Lamba, P. Singh, P. Singh, P. Singh, A. Bharti, M. Kumar, Y.K. Gupta, Recent advancements in supercapacitors based on different electrode materials: Classifications, synthesis methods and comparative performance, J Energy Storage 48 (2022) 103871.

[11] Y. Wang, L. Hao, Y. Zeng, X. Cao, H. Huang, J. Liu, X. Chen, S. Wei, L. Gan, P. Yang, M. Liu, D. Zhu, Three-dimensional hierarchical porous carbon derived from resorcinol formaldehyde-zinc tatrate/poly(styrene-maleic anhydride) for high performance supercapacitor electrode, J. Alloys Compd. 886 (2021) 161176.

[12] Y. Wang, Y. Zeng, J. Zhu, C. Yang, H. Huang, X. Chen, R. Wang, P. Yan, S. Wei, M. Liu, D. Zhu, From dual-aerogels with semi-interpenetrating polymer network structure to hierarchical porous carbons for advanced supercapacitor electrodes, Colloids Surfaces A Physicochem. Eng. Asp. 649 (2022) 129356.

[13] M.A. Garakani, S. Bellani, V. Pellegrini, R. Oropesa-Nuñez, A.E.D.R. Castillo, S. Abouali, L. Najafi, B. Martín-García, A. Ansaldo, P. Bondavalli, C. Demirci, V. Romano, E. Mantero, L. Marasco, M. Prato, G. Bracciale, F. Bonaccorso, Scalable spray-coated graphene-based electrodes for high-power electrochemical double-layer capacitors operating over a wide range of temperature, Energy Storage Mater. 34 (2021) 1–11.

[14] A. D'Alessandro, S. Bellani, A. Gamberini, V. Mastronardi, M.I. Zappia, M. Abruzzese, S. Thorat, E. Calcagno, F. Bonaccorso, Water-based supercapacitors with amino acid electrolytes: a green perspective for capacitance enhancement, Batter. Supercaps 7 (2024) e202300458.

[15] X. Jiao, J. Wang, Z. Yuan, C. Zhang, Smart current collector for high-energy-density and high-contrast electrochromic supercapacitors toward intelligent and wearable power application, Energy Storage Mater. 54 (2023) 254–265.

[16] Portfolio Management Energy from Smart Grid Deliverable: Report/white paper on Ultracapacitor technology Unlocking New Possibilities through Innovative Energy Storage The Role of Ultracapacitors in the Energy Transition, (2020). https://eit.europa.eu/sites/default/files/eitinnoenergy-frostsullivan_ultracapacitors_whitepaper_dec2020.pdf (accessed March 19, 2024).

[17] X. Zhang, B. Sun, X. Fan, P. Liang, G. Zhao, B.K. Saikia, X. Wei, Hierarchical porous carbon derived from coal and biomass for high performance supercapacitors, Fuel 311 (2022) 122552.

[18] M. Xiang, Y. Wang, J. Wu, Y. Guo, H. Wu, Y. Zhang, H. Liu, Natural Silk Cocoon Derived Nitrogen-doped Porous Carbon Nanosheets for High Performance Lithium-Sulfur Batteries, Electrochim. Acta 227 (2017) 7–16.

[19] J. Wang, Z. Li, S. Yan, X. Yu, Y. Ma, L. Ma, Modifying the microstructure of algae-based active carbon and modelling supercapacitors using artificial neural networks, RSC Adv. 9 (2019) 14797–14808.

[20] K. Slavik, C. Lemmen, W. Zhang, O. Kerimoglu, K. Klingbeil, K.W. Wirtz, The large-scale impact of offshore wind farm structures on pelagic primary productivity in the southern North Sea, Hydrobiologia 845 (2019) 35–53.

[21] R. Karlsson, M. Tivefälth, I. Duranović, S. Martinsson, A. Kjølhamar, K.M. Murvoll, Artificial hard-substrate colonisation in the offshore Hywind Scotland Pilot Park, Wind Energy Sci. 7 (2022) 801–814.

[22] H. Parsimehr, A. Ehsani, Algae-based electrochemical energy storage devices, Green Chem. 22 (2020) 8062–8096.

[23] A. Shchukarev, Z. Gojkovic, C. Funk, M. Ramstedt, Cryo-XPS analysis reveals surface composition of microalgae, Appl. Surf. Sci. 526 (2020) 146538.

[24] O. Norouzi, S. Taghavi, P. Arku, S. Jafarian, M. Signoretto, A. Dutta, What is the best catalyst for biomass pyrolysis? J. Anal. Appl. Pyrolysis 158 (2021) 105280.

[25] S. Zhang, J. Zheng, J. Wei, Y. Zhang, F. Niu, Y. Wang, H. Yan, Z. Li, C. Meng, Alkali etching zinc and manganese silicates derived from natural green algaes for supercapacitors with enhanced electrochemical properties, J. Colloid Interface Sci. 623 (2022) 135–145.

[26] P. Salimi, S. Tieuli, S. Taghavi, E. Venezia, S. Fugattini, S. Lauciello, M. Prato, S. Marras, T. Li, M. Signoretto, P. Costamagna, R. Proietti Zaccaria, Sustainable lithium-ion batteries based on metal-free tannery waste biochar, Green Chem. 24 (2022) 4119–4129.

[27] M. Ren, Z. Jia, Z. Tian, D. Lopez, J. Cai, M.M. Titirici, A.B. Jorge, High Performance N-Doped Carbon Electrodes Obtained via Hydrothermal Carbonization of Macroalgae for Supercapacitor Applications, ChemElectroChem 5 (2018) 2686–2693.

[28] B.R. Patra, A. Mukherjee, S. Nanda, A.K. Dalai, Biochar production, activation and adsorptive applications: a review, Environ. Chem. Lett. 19 (2021) 2237–2259.

[29] I. Yang, M. Jung, M.S. Kim, D. Choi, J.C. Jung, Physical and chemical activation mechanisms of carbon materials based on the microdomain model, J. Mater. Chem. A 9 (2021) 9815–9825.

[30] R. Ranguin, M. Delannoy, C. Yacou, C. Jean-Marius, C. Feidt, G. Rychen, S. Gaspard, Biochar and activated carbons preparation from invasive algae Sargassum spp. For Chlordecone availability reduction in contaminated soils, J. Environ Chem. Eng. 9 (2021) 105280.

[31] A.K. Sakhiya, A. Anand, P. Kaushal, Production, activation, and applications of biochar in recent times, Biochar 2 (2020) 253–285.

[32] C.L. Lee, P.S. H'Ng, M.T. Paridah, K.L. Chin, U. Rashid, M. Maminski, W.Z. Go, R. A. Raja Nazrin, S.N. Asyikin Rosli, P.S. Khoo, Production of bioadsorbent from phosphoric acid pretreated palm kernel shell and coconut shell by two-stage continuous physical activation via N_2 and air, R. Soc. Open Sci. 5 (2018) 180775.

[33] D. Robledo, E. Vázquez-Delfín, Y. Freile-Pelegrín, R.M. Vásquez-Elizondo, Z. N. Qui-Minet, A. Salazar-Garibay, Challenges and Opportunities in Relation to Sargassum Events Along the Caribbean Sea, Front. Mar. Sci. 8 (2021) 699664.

[34] A. Bagheri, S. Bellani, H. Beydaghi, M. Eredia, L. Najafi, G. Bianca, M.I. Zappia, M. Safarpour, M. Najafi, E. Mantero, Z. Sofer, G. Hou, V. Pellegrini, X. Feng, F. Bonaccorso, Functionalized Metallic 2D Transition Metal Dichalcogenide-Based Solid-State Electrolyte for Flexible All-Solid-State Supercapacitors, ACS Nano 16 (2022) 16426–16442.

[35] J.M. de la Rosa, M. Paneque, A.Z. Miller, H. Knicker, Relating physical and chemical properties of four different biochars and their application rate to biomass production of Lolium perenne on a Calcic Cambisol during a pot experiment of 79 days, Sci. Total Environ. 499 (2014) 175–184.

[36] B. Ma, Y. Huang, Z. Nie, X. Qiu, D. Su, G. Wang, J. Yuan, X. Xie, Z. Wu, Facile synthesis of: Camellia oleifera shell-derived hard carbon as an anode material for lithium-ion batteries, RSC Adv. 9 (2019) 20424–20431.

[37] S. Taghavi, O. Norouzi, A. Tavasoli, F. Di Maria, M. Signoretto, F. Menegazzo, A. Di Michele, Catalytic conversion of Venice lagoon brown marine algae for producing hydrogen-rich gas and valuable biochemical using algal biochar and Ni/SBA-15 catalyst, Int. J. Hydrogen Energy 43 (2018) 19918–19929.

[38] O. Farobie, A. Amrullah, A. Bayu, N. Syaftika, L.A. Anis, E. Hartulistiyoso, In-depth study of bio-oil and biochar production from macroalgae Sargassum sp. via slow pyrolysis, RSC Adv. 12 (2022) 9567–9578.

[39] W. Yu, H. Wang, S. Liu, N. Mao, X. Liu, J. Shi, W. Liu, S. Chen, X. Wang, N, O-codoped hierarchical porous carbons derived from algae for high-capacity supercapacitors and battery anodes, J. Mater. Chem. A 4 (2016) 5973–5983.

[40] N.R. Chodankar, S.J. Patil, S.K. Hwang, P.A. Shinde, S.V. Karekar, G.S.R. Raju, K. S. Ranjith, A.G. Olabi, D.P. Dubal, Y.S. Huh, Y.K. Han, Refurbished carbon materials from waste supercapacitors as industrial-grade electrodes: Empowering electronic waste, Energy Storage Mater. 49 (2022) 564–574.

[41] M. Gentile, S. Bellani, M.I. Zappia, A. Gamberini, V. Mastronardi, M. Abruzzese, L. Gabatel, L. Pasquale, S. Marras, A. Bagheri, H. Beydaghi, E.L. Papadopoulou, G. Lanzani, F. Bonaccorso, Hydrogen-Assisted Thermal Treatment of Electrode Materials for Electrochemical Double-Layer Capacitors, ACS Appl. Mater. Interfaces 16 (2024) 13706–13718.

[42] M.J. Matthews, M.A. Pimenta, G. Dresselhaus, M.S. Dresselhaus, M. Endo, Origin of dispersive effects of the Raman D band in carbon materials, Phys. Rev. B - Condens. Matter Mater. Phys. 59 (1999) 6585–6588.

[43] M.S. Dresselhaus, F. Villalpando-Paez, G.G. Samsonidze, S.G. Chou, G. Dresselhaus, J. Jiang, R. Saito, A.G. Souza Filho, A. Jorio, M. Endo, Y.A. Kim, Raman scattering from one-dimensional carbon systems, Phys. E Low-Dimensional Syst. Nanostructures 37 (2007) 81–87.

[44] A.C. Ferrari, J.C. Meyer, V. Scardaci, C. Casiraghi, M. Lazzeri, F. Mauri, S. Piscanec, D. Jiang, K.S. Novoselov, S. Roth, A.K. Geim, Raman spectrum of graphene and graphene layers, Phys. Rev. Lett. 97 (2006) 187401.

[45] M.A. Pimenta, G. Dresselhaus, M.S. Dresselhaus, L.G. Cançado, A. Jorio, R. Saito, Studying disorder in graphite-based systems by Raman spectroscopy, Phys. Chem. Chem. Phys. 9 (2007) 1276–1291.

[46] A.C. Ferrari, J. Robertson, Interpretation of Raman spectra of disordered and amorphous carbon, Phys. Rev. B 61 (2000) 14095.

[47] Y. Gao, R. Sun, A. Li, G. Ji, In-situ self-activation strategy toward highly porous biochar for supercapacitors: Direct carbonization of marine algae, J. Electroanal. Chem. 882 (2021) 114986.

[48] S. Taghavi, E. Ghedini, M. Peurla, G. Cruciani, F. Menegazzo, D. Yu, M. Signoretto, Activated biochars as sustainable and effective supports for hydrogenations, Carbon Trends 13 (2023) 100316.

[49] P. Manasa, S. Sambasivam, F. Ran, Recent progress on biomass waste derived activated carbon electrode materials for supercapacitors applications—A review, J. Energy Storage 54 (2022) 105290.

[50] X. Zhang, Y. Jiao, L. Sun, L. Wang, A. Wu, H. Yan, M. Meng, C. Tian, B. Jiang, H. Fu, GO-induced assembly of gelatin toward stacked layer-like porous carbon for advanced supercapacitors, Nanoscale 8 (2016) 2418–2427.

[51] Z. Tian, M. Xiang, J. Zhou, L. Hu, J. Cai, Nitrogen and Oxygen-Doped Hierarchical Porous Carbons from Algae Biomass: Direct Carbonization and Excellent Electrochemical Properties, Electrochim. Acta 211 (2016) 225–233.

[52] L. Longo, S. Taghavi, E. Ghedini, F. Menegazzo, A. Di Michele, G. Cruciani, M. Signoretto, Selective Hydrogenation of 5-Hydroxymethylfurfural to 1-Hydroxy-2,5-hexanedione by Biochar-Supported Ru Catalysts, ChemSusChem 15 (2022) e202200437.

[53] W. Chen, H. Yang, Y. Chen, M. Xia, X. Chen, H. Chen, Transformation of Nitrogen and Evolution of N-Containing Species during Algae Pyrolysis, Environ. Sci. Technol. 51 (2017) 6570–6579.

[54] W. Chen, H. Yang, Y. Chen, M. Xia, Z. Yang, X. Wang, H. Chen, Algae pyrolytic poly-generation: Influence of component difference and temperature on products characteristics, Energy 131 (2017) 1–12.

[55] W. Chen, H. Yang, Y. Chen, K. Li, M. Xia, H. Chen, Influence of Biochar Addition on Nitrogen Transformation during Copyrolysis of Algae and Lignocellulosic Biomass, Environ. Sci. Technol. 52 (2018) 9414–9521.
[56] S. Luryi, Quantum capacitance devices, Appl. Phys. Lett. 52 (1988) 501–503.
[57] H. Ji, X. Zhao, Z. Qiao, J. Jung, Y. Zhu, Y. Lu, L.L. Zhang, A.H. MacDonald, R. S. Ruoff, Capacitance of carbon-based electrical double-layer capacitors, Nat. Commun. 5 (2014) 3317.
[58] T. Sruthi, K. Tarafder, Enhancement of quantum capacitance by chemical modification of graphene supercapacitor electrodes: a study by first principles, Bull. Mater. Sci. 42 (2019) 257.
[59] K. Prasert, T. Sanglaow, M. Liangruksa, T. Sutthibutpong, Effects of stacking layers and different doping elements on the electronic structures and quantum capacitance of graphene: A DFT study, J. Phys. Chem. Solids 185 (2024) 111758.
[60] R. Shibuya, T. Kondo, J. Nakamura, Active sites in nitrogen-doped carbon materials for oxygen reduction reaction, Carbon-Based Met. Catal. Des. Appl. 1 (2018) 227–249.
[61] J. Li, X. Li, D. Xiong, Y. Hao, H. Kou, W. Liu, D. Li, Z. Niu, Novel iodine-doped reduced graphene oxide anode for sodium ion batteries, RSC Adv. 7 (2017) 55060–55066.
[62] L. Ge, Y. Wu, F. Wang, Y. Huang, Algae-Derived Nitrogen Self-Doped Porous Carbon Materials with High Supercapacitor Performances, Energy and Fuels 35 (2021) 15118–15125.
[63] O. Gerard, A. Numan, M.A.A.M. Abdah, M. Khalid, S. Ramesh, K. Ramesh, Rapid synthesis of nickel-copper phosphate electrode by microwave-assisted hydrothermal reaction for supercapattery, J. Energy Storage 61 (2023) 106813.
[64] M. Najafi, S. Bellani, V. Galli, M.I. Zappia, A. Bagheri, M. Safarpour, H. Beydaghi, M. Eredia, L. Pasquale, R. Carzino, S. Lauciello, J.-K.-K. Panda, R. Brescia, L. Gabatel, V. Pellegrini, F. Bonaccorso, Carbon-α-Fe_2O_3 Composite Active Material for High-Capacity Electrodes with High Mass Loading and Flat Current Collector for Quasi-Symmetric Supercapacitors, Electrochem 3 (2022) 463–478.
[65] Q. Zhang, S. Xu, Y. Wang, Q. Dou, Y. Sun, X. Yan, Temperature-dependent structure and performance evolution of “water-in-salt” electrolyte for supercapacitor, Energy Storage Mater. 55 (2023) 205–213.
[66] M. Eredia, S. Bellani, M.I. Zappia, L. Gabatel, V. Galli, A. Bagheri, H. Beydaghi, G. Bianca, I. Conticello, V. Pellegrini, F. Bonaccorso, High-energy density aqueous supercapacitors: The role of electrolyte pH and KI redox additive, APL Mater. 10 (2022) 101102.
[67] L. Najafi, S. Bellani, M.I. Zappia, M. Serri, R. Oropesa-Nuñez, A. Bagheri, H. Beydaghi, R. Brescia, L. Pasquale, D.V. Shinde, Y. Zuo, F. Drago, K. Mosina, Z. Sofer, L. Manna, F. Bonaccorso, Transition metal dichalcogenides as catalysts for the hydrogen evolution reaction: The emblematic case of “inert” $ZrSe_2$ as catalyst for electrolyzers, Nano Sel. 3 (2022) 1069–1081.
[68] G. Vignesh, R. Ranjithkumar, P. Devendran, N. Nallamuthu, S. Sudhahar, M. Krishna Kumar, Nitrogen doped reduced graphene oxide/$ZnCo_2O_4$ nanocomposite electrode for hybrid supercapacitor application, Mater. Sci. Eng. B Solid-State Mater. Adv. Technol. 290 (2023) 116328.
[69] Q. Abbas, B. Gollas, V. Presser, Reduced Faradaic Contributions and Fast Charging of Nanoporous Carbon Electrodes in a Concentrated Sodium Nitrate Aqueous Electrolyte for Supercapacitors, Energy Technol. 7 (2019) 1900430.
[70] M.F. El-Kady, M. Ihns, M. Li, J.Y. Hwang, M.F. Mousavi, L. Chaney, A.T. Lech, R. B. Kaner, Engineering three-dimensional hybrid supercapacitors and microsupercapacitors for high-performance integrated energy storage, Proc. Natl. Acad. Sci. u. s. a. 112 (2015) 4233–4238.
[71] L. Liu, J. Niu, Z. Zhang, F. Wang, Co-activation Pore Engineering of Polyphthalocyanine-Derived Carbon Nanosheets for Supercapacitors in Organic Electrolytes, ACS Appl. Energy Mater. 4 (2021) 7751–7758.
[72] Y.G. Cho, C. Hwang, D.S. Cheong, Y.S. Kim, H.K. Song, Gel/Solid Polymer Electrolytes Characterized by In Situ Gelation or Polymerization for Electrochemical Energy Systems, Adv. Mater. 31 (2019) 1804909.
[73] W. Qin, N. Zhou, C. Wu, M. Xie, H. Sun, Y. Guo, L. Pan, Mini-Review on the Redox Additives in Aqueous Electrolyte for High Performance Supercapacitors, ACS Omega 5 (2020) 3801–3808.
[74] K. Gajewska, A. Moyseowicz, D. Minta, G. Gryglewicz, Effect of electrolyte and carbon material on the electrochemical performance of high-voltage aqueous symmetric supercapacitors, J. Mater. Sci. 58 (2023) 1721–1738.
[75] X. Gao, J. Yang, Z. Xu, Y. Nuli, J. Wang, Recent progress of aqueous and organic/aqueous hybrid electrolytes for low-temperature rechargeable metal-ion batteries and supercapacitors, Energy Storage Mater. 54 (2023) 382–402.
[76] B. Tansel, Significance of thermodynamic and physical characteristics on permeation of ions during membrane separation: Hydrated radius, hydration free energy and viscous effects, Sep. Purif. Technol. 86 (2012) 119–126.
[77] D. DeRosa, S. Higashiya, A. Schulz, M. Rane-Fondacaro, P. Haldar, High performance spiro ammonium electrolyte for Electric Double Layer Capacitors, J. Power Sources 360 (2017) 41–47.
[78] C. Decaux, C. Matei Ghimbeu, M. Dahbi, M. Anouti, D. Lemordant, F. Béguin, C. Vix-Guterl, E. Raymundo-Piñero, Influence of electrolyte ion-solvent interactions on the performances of supercapacitors porous carbon electrodes, J. Power Sources 263 (2014) 130–140.
[79] C. Zhong, Y. Deng, W. Hu, J. Qiao, L. Zhang, J. Zhang, A review of electrolyte materials and compositions for electrochemical supercapacitors, Chem. Soc. Rev. 44 (2015) 7484–7539.
[80] Z. Chen, X. Wang, Z. Ding, Q. Wei, Z. Wang, X. Yang, J. Qiu, Biomass-based Hierarchical Porous Carbon for Supercapacitors: Effect of Aqueous and Organic Electrolytes on the Electrochemical Performance, ChemSusChem 12 (2019) 5099–5110.
[81] S.W. Xu, Y.Q. Zhao, Y.X. Xu, Q.H. Chen, G.Q. Zhang, Q.Q. Xu, D.D. Zhao, X. Zhang, C.L. Xu, Heteroatom doped porous carbon sheets derived from protein-rich wheat gluten for supercapacitors: The synergistic effect of pore properties and heteroatom on the electrochemical performance in different electrolytes, J. Power Sources 401 (2018) 375–385.
[82] J. Wang, P. Zhang, L. Liu, Y. Zhang, J. Yang, Z. Zeng, S. Deng, Controllable synthesis of bifunctional porous carbon for efficient gas-mixture separation and high-performance supercapacitor, Chem. Eng. J. 348 (2018) 57–66.
[83] H. Zhang, T. Wang, Z. Sui, Y. Zhang, B. Sun, W.P. Pan, Enhanced mercury removal by transplanting sulfur-containing functional groups to biochar through plasma, Fuel 253 (2019) 703–712.
[84] N.R. Chodankar, P.A. Shinde, S.J. Patil, S.K. Hwang, G.S.R. Raju, K.S. Ranjith, D. P. Dubal, Y.S. Huh, Y.K. Han, Solution-free self-assembled growth of ordered tricopper phosphide for efficient and stable hybrid supercapacitor, Energy Storage Mater. 39 (2021) 194–202.
[85] M.A. Aziz, S.S. Shah, S.M.A. Nayem, M.N. Shaikh, A.S. Hakeem, I.A. Bakare, Peat soil-derived silica doped porous graphitic carbon with high yield for high-performance all-solid-state symmetric supercapacitors, J. Energy Storage 50 (2022) 104278.
[86] R. Ma, X. Zhang, J. Zhuo, L. Cao, Y. Song, Y. Yin, X. Wang, G. Yang, F. Yi, Self-Supporting, Binder-Free, and Flexible $Ti_3C_2T_x$ MXene-Based Supercapacitor Electrode with Improved Electrochemical Performance, ACS Nano 16 (2022) 9713–9727.
[87] D. Cericola, R. Kötz, A. Wokaun, Effect of electrode mass ratio on aging of activated carbon based supercapacitors utilizing organic electrolytes, J. Power Sources 196 (2011) 3114–3118.
[88] V.I. Volkov, A.V. Chernyak, D.V. Golubenko, V.A. Tverskoy, G.A. Lochin, E. S. Odjigaeva, A.B. Yaroslavtsev, Hydration and diffusion of H^+, Li^+, Na^+, Cs^+ ions in cation-exchange membranes based on polyethylene-and sulfonated-grafted polystyrene studied by nmr technique and ionic conductivity measurements, Membranes 10 (2020) 272.
[89] L.V. Karpenko-Jereb, A.M. Kelterer, N.P. Berezina, A.V. Pimenov, Conductometric and computational study of cationic polymer membranes in H^+ and Na^+-forms at various hydration levels, J. Memb. Sci. 444 (2013) 127–138.
[90] A. Bagheri, M. Javanbakht, P. Hosseinabadi, H. Beydaghi, A. Shabanikia, Preparation and characterization of SPEEK/SPVDF-co-HFP/$LaCrO_3$ nanocomposite blend membranes for direct methanol fuel cells, Polymer 138 (2018) 275–287.
[91] T.S. Mathis, N. Kurra, X. Wang, D. Pinto, P. Simon, Y. Gogotsi, Energy Storage Data Reporting in Perspective—Guidelines for Interpreting the Performance of Electrochemical Energy Storage Systems, Adv. Energy Mater. 9 (2019) 1902007.
[92] M. Majumder, M.S. Santosh, R. Viswanatha, A.K. Thakur, D.P. Dubal, K. Jayaramulu, Two-dimensional Conducting Metal-Organic Frameworks Enabled Energy Storage Devices, Energy Storage Mater. 37 (2021) 396–416.